

# Signatures of Cool Gas Fueling a Star-Forming Galaxy at Redshift 2.3

N. Bouché<sup>1,2,\*</sup>, M. T. Murphy<sup>3</sup>, G. G. Kacprzak<sup>3</sup>, C. Péroux<sup>4</sup>,  
T. Contini<sup>1,2</sup>, C. L. Martin<sup>5</sup>, M. Dessauges-Zavadsky<sup>6</sup>

<sup>1</sup>CNRS/IRAP, 14 Avenue E. Belin, F-31400 Toulouse, France

<sup>2</sup>University Paul Sabatier of Toulouse/ UPS-OMP/ IRAP, F-31400 Toulouse, France

<sup>3</sup>Swinburne University of Technology, PO Box 218, Hawthorn, Victoria 3122, Australia

<sup>4</sup>Aix Marseille Université, CNRS, LAM (Laboratoire d'Astrophysique de Marseille) UMR 7326,  
F-13388 Marseille, France

<sup>5</sup>Department of Physics, University of California, Santa Barbara, CA 93106, USA

<sup>6</sup>Observatory of Geneva, 51 chemin des Maillettes, CH-1290 Versoix, Switzerland

\*To whom correspondence should be addressed. E-mail: nicolas.bouche@irap.omp.eu.

**Galaxies are thought to be fed by the continuous accretion of intergalactic gas, but direct observational evidence has been elusive. The accreted gas is expected to orbit about the galaxy's halo, delivering not just fuel for star-formation but also angular momentum to the galaxy, leading to distinct kinematic signatures. We report observations showing these distinct signatures near a typical distant star-forming galaxy where the gas is detected using a background quasar passing 26 kpc from the host. Our observations indicate that gas accretion plays a major role in galaxy growth since the estimated accretion rate is comparable to the star-formation rate.**

At all epochs, galaxies have short gas depletion time scales ( $1, 2$ ); to sustain the observed levels of star-formation over many billions of years, galaxies must continuously replenish their gas

reservoir with fresh gas accreted from the vast amounts available in the intergalactic medium. In numerical cosmological simulations (3–5), the accretion phenomenon is often referred to as ‘cold accretion’ (6) and this term describes the mass regime where the accretion is most efficient (7, 8). The cold accreted gas should orbit about the halo before falling in to build the central disk, delivering fuel for star formation and also angular momentum to shape the outer parts of the galaxy (9, 10). Thus, accreting material should co-rotate with the central disk in the form of a warped, extended cold gaseous disk, producing distinct kinematic signatures in absorption systems. In particular, the gas kinematics are expected to be offset by about  $100 \text{ km s}^{-1}$  from the galaxy’s systemic velocity and these kinematic signatures of gas accretion should be observable in suitable quasar absorption line systems (6, 11–13).

Here, we describe observations of a background quasar whose apparent location on the sky is fortuitously aligned with the galaxy’s projected major-axis, making it possible to test these predictions. The associated star-forming galaxy with redshift  $z = 2.3285$  is located just 26 kpc from the damped Lyman absorber (DLA) seen towards the quasar HE 2243–60 (14). The galaxy was detected in our  $z \simeq 2$  SINFONI (15) survey called the SINFONI MgII Program for Line Emitters (SIMPLE) (16). Recent adaptive optics (AO) assisted SINFONI observations (17) of this  $z = 2.3285$  star-forming galaxy (Fig. 1a) obtained at the Very Large Telescope (VLT) with  $\sim 1 \text{ kpc}$  (0.25 arc sec) resolution (table S1) allow us to map the emission kinematics with precision (Fig. 1b and figs S3 and S4). The kinematics reveal that this galaxy has physical properties (Table 1) typical for rotationally-supported disks seen at that redshift (18). For instance, the galaxy has a star-formation rate (SFR) of  $33_{-11}^{+40} M_{\odot} \text{ year}^{-1}$  (where  $M_{\odot}$  is the mass of the Sun), its maximum rotation velocity is  $150 \pm 15 \text{ km s}^{-1}$  from 3D fitting (Fig. S4, Table S3), and its metallicity is about 1/2 solar ( $[\text{O}/\text{H}] = -0.35 \pm 0.1 \text{ dex}$ ) determined from a joint fit to all the major nebular emission lines ( $[\text{O II}]$ ,  $[\text{O III}] + \text{H}\beta$  and  $\text{H}\alpha/[\text{N II}]$ ; figs. S1 and S2).

Analysis of a deep high-resolution VLT/UVES (Ultraviolet and Visual Echelle Spectro-

graph) spectrum of the background quasar HE 2243–60 (fig. S5) (17) shows that the gas metallicity can give us insights into the physical nature of the gas. In particular, the total HI column is  $\log(N_{\text{H}}/\text{cm}^{-2}) \simeq 20.6$  (i.e. almost entirely neutral) and, from the undepleted low-ionisation ion Zn II, the gas metallicity ( $[\text{Zn}/\text{H}] = -0.72 \pm 0.05$ ) is much lower than that of the galaxy ( $[\text{O}/\text{H}] = -0.35 \pm 0.1$  dex). This comparison disfavor an outflow scenario because these tend to be metal rich (19). Moreover, a bi-conical outflow should have a very wide cone opening angle ( $> 140^\circ$ ) in order to intercept the quasar line-of-sight given the galaxy inclination of 55 deg (Fig. S6). Such a wide cone would result in a very large covering fraction, not supported by DLA host statistics, and would not be compatible with the current constraints on opening angles for outflows near star-forming galaxies at  $z = 0.1$  to 1 (20–22).

The kinematics of the absorbing gas give us more clues about the nature of the gas. Thanks to our VLT/SINFONI-AO observations giving us the orientation of the galaxy with respect to the line-of-sight, the gas kinematics show distinct features (Fig. 1, fig. S5), and these features can be put in the broader context of the host galaxy kinematics. For instance, the gas seen in absorption 26 kpc from the galaxy — corresponding to 7 times the half-light radius  $R_{1/2} = 3.6$  kpc or one third of the virial size of the halo  $R_{\text{vir}}$  — is moving in the same direction as the galaxy rotation; that is, the gas appears to be co-rotating. Indeed, the observed velocity field of this rotating galaxy (Fig. 1b) shows redshifted velocities in the direction of the quasar location, and in the quasar spectrum all of the low-ionization ions Zn II, Cr II, Fe II and Si II tracing the cold gas also show redshifted velocities (Fig. 1c).

Thanks to the apparent quasar location on the sky being only  $10^\circ$  to  $20^\circ$  from the galaxy’s projected major-axis, we can identify two distinct features in the low-ionisation lines. The first feature comes from a quantitative comparison between the velocity field of the galaxy (Fig. 1b) and the low-ionization kinematics (Fig. 1c): The velocities seen in absorption for component 4 and seen in emission from the galaxy closely match one another. This would indicate that

a simple rotating disk with circular orbits and a normal (flat) rotation curve can account for the bulk of the absorbing gas kinematics, but not all. Thus, components 1 to 3 which have a line-of-sight velocity less than the rotation speed correspond to gas that is also co-rotating, but that is not rotationally supported because these components do not have the required speed. In other words, two groups of components (1 to 3; 4 to 6) are seen and one group is offset by about  $100\text{km s}^{-1}$  from the rotation pattern; hence this group cannot be gravitationally supported and therefore should be flowing in. Each of these two groups contain about half of the total HI column  $\log N_{\text{H}} \simeq 20.6$  (fig. S5) (17).

Thus, our SINFONI and UVES data show that the absorbing components have the broad characteristics of low-metallicity, co-planar, co-rotating accreting material similar to the expected features from numerical simulations (9). Moreover, the dust profile (fig. S5D) determined from the data (17) indicates that components 1 to 3 are less enriched than the main components (4 & 5). Given that the amount of dust (or dust-to-gas ratio) correlates with the metallicity (23), the dust profile also supports the scenario in which the quasar line-of-sight probes a mix of accreting material with that of an extended gaseous disk.

To gain further insights into the accreting gas, we experimented with a simple geometrical toy model using a Monte Carlo approach to generate simulated absorption profiles (17). In the model, we distribute “particles” representing gas clouds or absorption components where the cloud kinematics reflect an inflowing gas (radial for simplicity, see Fig. 2). Because the relative galaxy orientation is well determined by the VLT/SINFONI data, the only free parameter is the inflow speed (fig. S6). The resulting absorption profile simulated at the UVES resolution (Fig. 1D) shows qualitative agreement with the data (Fig. 1C).

We do not expect such a model to be completely realistic nor to fit the data perfectly; there are many uncertainties such as the exact geometry of the accreting gas. However, the model can give us a framework to estimate the amount of accretion (17). The accreting material coming

from the large-scale filamentary structure is presumed to form a roughly co-planar structure around the galaxy (9, 10). Assuming an azimuthal symmetry (see Fig. 2 and fig. S6), the global mass flux rate through an area of  $2\pi b h_z$  is thus

$$\begin{aligned} \dot{M}_{\text{in}}(b) &\propto 2\pi N_{\text{H}} b V_{\text{in}} \cos(i), \\ &= 46 \left(\frac{\mu}{1.6}\right) \left(\frac{N_{\text{H}}}{2 \times 10^{20} \text{ cm}^{-2}}\right) \left(\frac{b}{26 \text{ kpc}}\right) \left(\frac{V_{\text{in}}}{200 \text{ km/s}}\right) \left(\frac{\cos(i)}{0.57}\right) M_{\odot} \text{ year}^{-1} \end{aligned} \quad (1)$$

where  $\mu$  is the mean molecular weight,  $N_{\text{H}}$  is the gas column,  $b$  the impact parameter,  $V_{\text{in}}$  is the radial velocity component and  $i$  is the disk inclination. This expression holds for any thin structure of thickness  $h_z$  and density  $\rho$  because we used the identity  $N_{\text{H}} = \int dz \rho(b) = \rho(b) h_z / \cos(i)$ .

Using the constraints on  $V_{\text{in}}$  and on  $N_{\text{H}}$  from our SINFONI and UVES data set, the estimated mass flux  $\dot{M}_{\text{in}}$  in cold gas is around 30 to 60  $M_{\odot} \text{ year}^{-1}$  given the uncertainties in the column density and inflow speed. This accretion rate could be overestimated if the flow is very asymmetric and more realistic models with spiral orbits will lead to results that may differ by the cosine of the spiral opening angle, leading to (downward) corrections by factors of 2 to 3. Similarly, if we relax our assumption of a flat HI profile, the gas column density must be higher for components 1 to 3 to account for both the dust profile and the Si II column density, leading to an upward correction to the accretion rate.

The range of accretion rates estimated from Eq. 1, 30 to 60  $M_{\odot} \text{ year}^{-1}$ , is found to be close to the galaxy's SFR of  $\sim 33_{-11}^{+40} M_{\odot} \text{ year}^{-1}$ . This is in agreement with the simplest arguments for galaxy growth via self-regulation (24, 25) and from numerical simulations (4, 6). Furthermore, for this galaxy's halo mass,  $M_h \sim 4 \times 10^{11} M_{\odot}$  (determined from its rotation curve), this value of  $\dot{M}_{\text{in}}$  corresponds to an accretion efficiency  $\epsilon$  of  $\sim 100\%$  [where  $\epsilon$  is defined as the ratio between the observed and maximum expected baryonic accretion rate, namely  $\epsilon \equiv \dot{M}_{\text{in}} / (f_B \dot{M}_h)$ , where  $f_B$  is the universal baryonic fraction and  $\dot{M}_h$  the halo growth rate (26, 27)].

Our study shows the potential of the technique of using background quasars passing near galaxies to further understand the process of gas accretion in galaxies. This technique is complementary to other recent studies (28–30). Our observations, which are merely consistent with cold accretion, provide key evidence important to consider against hydro-dynamical simulations.

## References

1. E. Daddi, *et al.*, *ApJ* **713**, 686 (2010).
2. R. Genzel, *et al.*, *MNRAS* **407**, 2091 (2010).
3. D. Kereš, N. Katz, D. H. Weinberg, R. Davé, *MNRAS* **363**, 2 (2005).
4. C.-A. Faucher-Giguère, D. Kereš, C.-P. Ma, *MNRAS* **417**, 2982 (2011).
5. F. van de Voort, J. Schaye, C. M. Booth, M. R. Haas, C. Dalla Vecchia, *MNRAS* **414**, 2458 (2011).
6. A. Dekel, *et al.*, *Nat* **457**, 451 (2009).
7. S. D. M. White, C. S. Frenk, *ApJ* **379**, 52 (1991).
8. Y. Birnboim, A. Dekel, *MNRAS* **345**, 349 (2003).
9. K. R. Stewart, *et al.*, *ApJ* **738**, 39 (2011).
10. S. Shen, *et al.*, *ApJ* **765**, 89 (2013).
11. K. R. Stewart, *et al.*, *ApJ* **735**, L1+ (2011).
12. M. Fumagalli, *et al.*, *MNRAS* **418**, 1796 (2011).

13. T. Goerdt, A. Dekel, A. Sternberg, O. Gnat, D. Ceverino, *MNRAS* **424**, 2292 (2012).
14. S. Lopez, D. Reimers, S. D’Odorico, J. X. Prochaska, *A&A* **385**, 778 (2002).
15. SINFONI is the near-infrared integral field spectrograph at one of the Very Large Telescopes (VLTs) of the European Southern Observatory (ESO).
16. N. Bouché, *et al.*, *MNRAS* **419**, 2 (2012).
17. See supporting material in Science online.
18. N. M. Förster Schreiber, *et al.*, *ApJ* **706**, 1364 (2009).
19. T. Tripp, *et al.*, *Sc.* **334** 952 (2011).
20. R. Bordoloi, *et al.*, *ApJ* **743**, 10 (2011).
21. N. Bouché, *et al.*, *MNRAS* **426**, 801 (2012).
22. G. Kacprzak, *et al.*, *ApJ*, **760**, 7 (2012)
23. G. Vladilo, *et al.*, *A&A* **454**, 151 (2006).
24. A. A. Dutton, F. C. van den Bosch, A. Dekel, *MNRAS* **405**, 1690 (2010).
25. N. Bouché, *et al.*, *ApJ* **718**, 1001 (2010).
26. S. Genel, *et al.*, *ApJ* **688**, 789 (2008).
27. J. McBride, O. Fakhouri, C. Ma, *MNRAS* **398**, 1858 (2009).
28. M. Giavalisco, *et al.*, *ApJ* **743**, 95 (2011).
29. K. H. R. Rubin, J. X. Prochaska, D. C. Koo, A. C. Phillips, *ApJ* **747**, L26 (2012).
30. J. Ribaud, *et al.*, *ApJ* **743**, 207 (2011).

## Acknowledgments

We thank the ESO Paranal staff for their continuous support and the SINFONI instrument team for their hard work which made SINFONI a very reliable instrument. NB thanks S. Lilly and R. Bordoloi for stimulating discussions and S. Genel for a careful read of the manuscript. We thank I. Schroetter for his assistance in making Figure 2. We thank the reviewers for their thorough review, their comments and suggestions. This research was based upon work supported in part by the National Science Foundation under grant No. 1066293 and the hospitality of the Aspen Center for Physics. It was partly supported by a Marie Curie International Outgoing Fellowship (PIOF-GA-2009-236012) and by a Marie Curie International Career Integration Grant (PCIG11-GA-2012-321702) within the 7th European Community Framework Program. M.T.M thanks the Australian Research Council for a *QEII Fellowship* (DP0877998) and *Discovery Project* grant (DP130100568). C.L.M. is supported by NSF grant AST-1109288. The data used in this paper are tabulated in the Supporting Online Material and archived at <http://archive.eso.org> under program ID 383.A-0750 and 088.B-0715. G.G.K. is an Australian Research Council Super Science Fellow.



**Fig. 1** Emission and Absorption Kinematics. **(a)** The color scale represents a narrow band image (rest-frame  $H\alpha$ ) with the continuum subtracted from our AO-assisted VLT/SINFONI datacube. The quasar HE2243–60 and the host  $z \sim 2.328$  galaxy are marked. The residuals from the continuum subtraction are visible both near the QSO and near the position labeled R. The galaxy is detected in  $H\alpha$  with a maximum SNR of  $\sim 5$ –8 per pixel; no continuum emission is detected. The beam has a full-width-at-half-maximum (FWHM) of  $\sim 0.25$  arc sec. **(b)** The fitted velocity field (extrapolated over the entire field) is shown along with the flux contours. The kinematic parameters were determined using our 3D analysis (17). The dotted line shows the kinematic major axis. At the quasar location (solid circle), the rotation speed is expected to be  $\sim 160$  to  $180 \text{ km s}^{-1}$ . **(c)** The absorption profiles from the VLT/UVES spectra showing the line-of-sight velocity of the various absorption components in the low-ionization ion (ZnII, CrII, NiII, FeII and SiII) where  $v = 0 \text{ km s}^{-1}$  corresponds to the galaxy redshift. The main component (component 4) contains half of the SiII column density and appears to contain more dust (17). This component has a line-of-sight velocity  $v = 180 \text{ km s}^{-1}$  consistent with that of the galaxy velocity field shown in (a). **(d)** A simulated line-of-sight profile for the geometry of this QSO-galaxy pair from a toy model that includes an inflow component (black) in addition to a component determined from the extended galaxy velocity field (red). A schematic representation of the model is shown in Fig. 2 and a more detailed representation is presented in fig. S6.

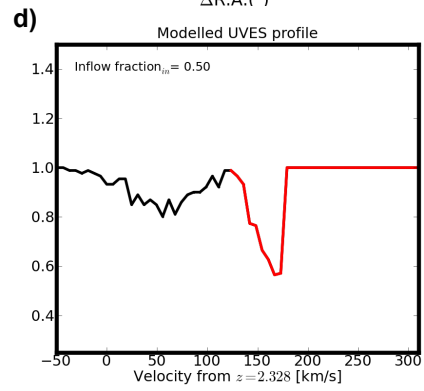
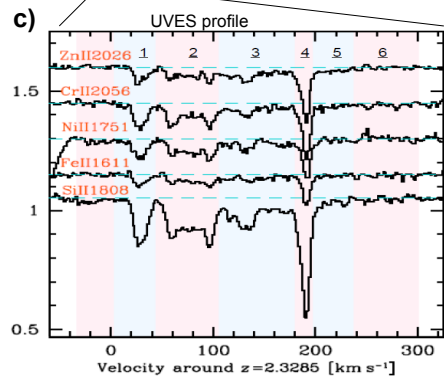
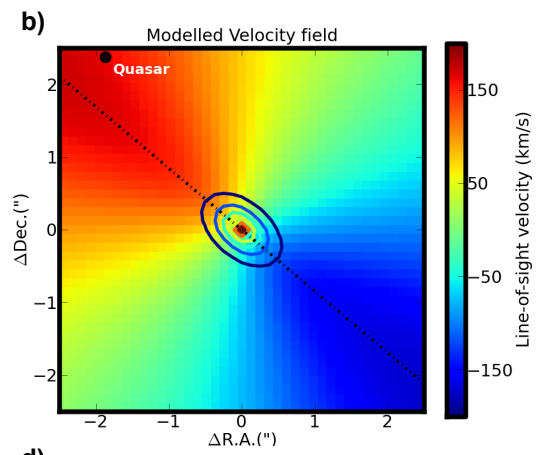
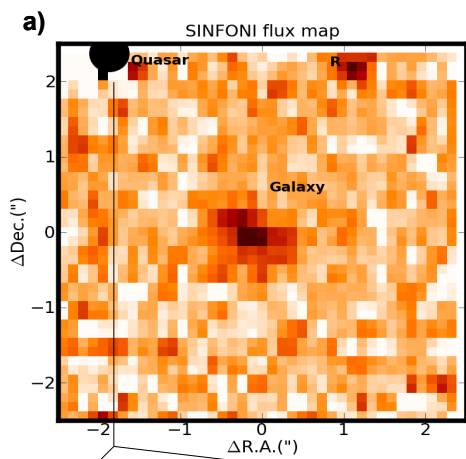


**Fig. 2** Schematic diagram of the simplified model. The star-forming galaxy is experiencing a super-nova driven outflow (red) and receiving gas with low angular momentum from the intergalactic medium (blue). The opening angle of the bi-polar outflow is assumed to be approximately  $60^\circ$ , as found in low-redshift observations (20–22). The accreting cold gas is expected to dissipate its angular momentum and migrate towards the galaxy, delivering fuel for the galaxy and forming an extended gaseous co-planar structure. The quasar (yellow) line of sight is represented by the star and is about  $\alpha = 20^\circ$  from the major-axis leading to distinct kinematic features seen in the absorption spectra (Fig 1d; fig. S6). For the observed geometric configuration, the line-of-sight is intercepting the accreting material but not the outflowing material.

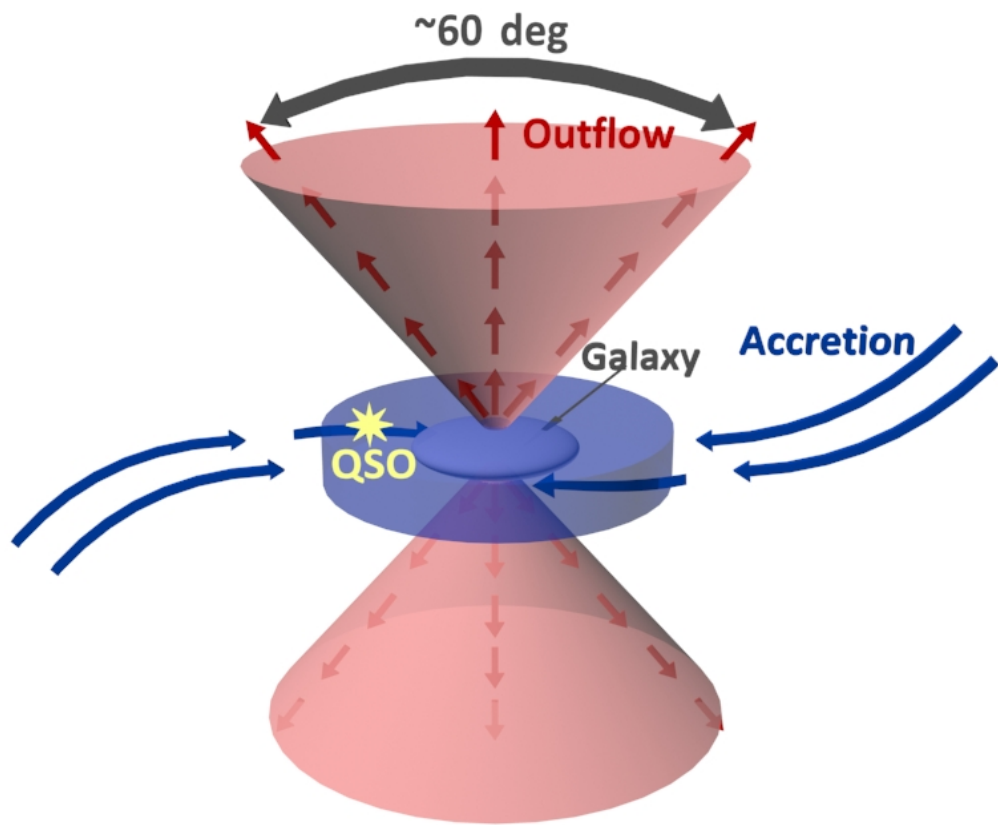


Table 1: Physical properties of the galaxy

Quasar Impact Parameter ( $b$ )	$3.1''$ or 26 kpc
Major-Axis position angle	$62 \pm 5^\circ$
Quasar position angle	$42 \pm 1^\circ$
Redshift $z_{\text{H}\alpha}$	$2.3283 \pm 0.0001$
Half-Light Radius ( $R_{1/2}$ )	$3.6 \pm 0.3$ kpc
Maximum Circular Velocity ( $V_{\text{max}}$ )	$150 \pm 15$ km s $^{-1}$
Inclination ( $i$ )	$55 \pm 1^\circ$
Dispersion Velocity ( $\sigma_i$ )	$158 \pm 5$ km s $^{-1}$
Halo Mass ( $M_h$ )	$\sim 4 \times 10^{11} M_\odot$
Virial Radius ( $R_{\text{vir}}$ )	$\sim 90$ kpc
Dynamical Mass <sup>1</sup> ( $M_{\text{dyn}}$ )	$2.0 \times 10^{10} M_\odot$
Interstellar Gas Mass <sup>2</sup> ( $M_g$ )	$1.5 \times 10^{10} M_\odot$
Gas fraction ( $f_g$ )	$\sim 0.75$
Metallicity ( $\log Z/Z_\odot$ )	$-0.35 \pm 0.1$
SFR $_{\text{H}\alpha}$ <sup>3</sup>	$18 \pm 2 M_\odot \text{ year}^{-1}$
Dust corrected SFR $_{\text{H}\alpha}$	$33^{+40}_{-11} M_\odot \text{ year}^{-1}$
Gas Accretion Rate ( $\dot{M}_{\text{in}}$ )	$\sim 45 M_\odot \text{ year}^{-1}$

<sup>1</sup>Within the half-light radius  $r_{1/2}$  assuming  $V_c^2 = G M/r_{1/2}$ .

<sup>2</sup>Within the half-light radius  $r_{1/2}$  determined from the H $\alpha$  surface density by inverting the star-formation law.

<sup>3</sup>Integrated SFR (17).

# Supplementary Online Materials for

## Signatures of Cool Gas Fueling a Star-Forming Galaxy at Redshift 2.3

N. Bouché\*, M. T. Murphy, G. G. Kacprzak, C. Péroux,

T. Contini, C. L. Martin, M. Dessauges-Zavadsky

\*To whom correspondence should be addressed. E-mail: nicolas.bouche@irap.omp.eu.

### **This pdf includes:**

Supporting Online Material:

Figs. S1–S6

Tables S1–S4

References 31–73

In this Supporting Online Materials we provide additional details on the data sets and the data analysis regarding the accretion of cool gas near a  $z \sim 2.3$  star-forming galaxy. In section § S1, we describe the VLT/SINFONI observations and we present our 3D kinematic analysis. In section § S2, we describe the VLT/UVES observations and present the absorbing gas kinematics seen along the quasar line-of-sight. In section § S3, we present more information regarding the toy model used in the main text. Throughout, we use the following cosmological parameters  $h = 0.7$ ,  $\Omega_M = 0.3$ , and  $\Omega_\Lambda = 0.7$ .

## S1 Galaxy emission properties

### S1.1 SINFONI/VLT Integral Field Spectroscopy

The star-forming galaxy is associated with a damped Ly $\alpha$  absorber (DLA) with a neutral hydrogen column density  $N_{\text{HI}}$  of  $\log[N_{\text{HI}}/\text{cm}^{-2}] = 20.62 \pm 0.05$  and was found 26 kpc (3.1'') away from the quasar HE 2243–60 in seeing-limited VLT/SINFONI observations (16). In this study, we use recent VLT/SINFONI observations, obtained in service mode between 2009 and 2011 (see Table S1). In order to ensure the highest spatial resolution possible the observations were taken using Adaptive Optics (AO) with the quasar as a Natural Guide Star (NGS). The field was observed in all three gratings ( $J$ ,  $H$ , and  $K$ ), covering all the nebular lines [O II], [O III]+H $\beta$  and H $\alpha$ +[N II]. We used the 0.125'' pixel scale in all three gratings to maximize the surface-brightness sensitivity. The total integration times were 12ks, 12ks and 10.8ks in  $K$ ,  $H$ , and  $J$  respectively. The full-width-at-half-max (FWHM) of the point spread functions (PSF) are 0.25'', 0.4'' and 0.65'' in  $K$ ,  $H$  and  $J$  respectively. The data reduction was performed using the MPE SINFONI pipeline (31, 32) complemented with additional routines designed to optimize the subtraction of the OH sky lines (33). In addition, we applied the heliocentric correction to the individual cubes before combining them to a single cube. The flux calibration of the data was performed using the 2MASS broadband magnitudes of standard stars ( $O$  or  $B$  stars), which yields a calibration accurate to  $\sim 15\%$ . The full description of the reduction steps is described elsewhere (16, 18, 34, 35).

### S1.2 Flux, Metallicity and Size measurements

Figure S1 shows the one-dimensional spectra extracted in a 1.25'' radius aperture for each of the nebular lines. We fitted each of the emission lines with Gaussian line profiles. The two components of the [O III] and [O II] doublets are fitted simultaneously. The [N II] $\lambda$ 6584 emission line is fitted jointly with the H $\alpha$  line (with the reshift and dispersion joined), and the [N II] $\lambda$ 6584 flux should be treated as an upper limit. The [N II] flux is  $< 1.2 \times 10^{-17} \text{ erg s}^{-1} \text{ cm}^{-2}$ . Similarly, the H $\beta$  flux is determined from a joint [O III]+H $\beta$  fit where the centroid and line width (FWHM) are tied. The flux measurements are summarized in Table S3. From the H $\alpha$  flux of  $9.1 \pm 0.3 \times 10^{-17} \text{ erg s}^{-1} \text{ cm}^{-2}$ , we infer an observed SFR of  $\sim 18 \pm 2 M_\odot \text{ year}^{-1}$  for a Chabrier

Initial Mass Function (IMF) (36), and a dust-corrected intrinsic  $\text{SFR}_0$  of  $\sim 30 \pm 5 M_\odot \text{ year}^{-1}$ , using  $E(B - V) \simeq 0.25$  estimated below and a Calzetti extinction curve (37). The [OIII] flux is  $8.1 \pm 0.4 \times 10^{-17} \text{ erg s}^{-1} \text{ cm}^{-2}$ . We find that the  $\text{H}\beta$  flux is  $1.7 \pm 0.4 \times 10^{-17} \text{ erg s}^{-1} \text{ cm}^{-2}$ . The [OII] flux is  $3.8 \pm 0.4 \times 10^{-17} \text{ erg s}^{-1} \text{ cm}^{-2}$ . See Table S2 for the summary of the flux measurements.

With our [OII], [OIII]+ $\text{H}\beta$ , and [NII]+ $\text{H}\alpha$  flux measurements we can determine the metallicity of the host using the five common metallicity indicators (R23, O3O2, O3Hb, O2Hb, N2) (38). Because the [NII] line is only hinted in the data (see Figure S1) and the R23 indicator is double-valued, the tightest constraint comes from O3O2. We use a simultaneous fit to the five indicators to determine the metallicity  $Z$  and the amount of extinction  $A_V$  (39). Figure S2 shows that the metallicity of the host towards HE 2243–60 is

$$12 + \log \frac{O}{H} = 8.34 \pm 0.10 \quad (2)$$

corresponding to a metallicity of  $Z = -0.35 \pm 0.1$  using solar abundance  $Z_\odot = 8.69$  (40), which is typical for galaxies at  $z \gtrsim 2$  (41, 42). In other words, the galaxy seems to lie on the mass–metallicity sequence and we find no evidence for a metallicity gradient from the emission line galaxy data. From our global fit to the line fluxes, the extinction is found to be  $E(B - V) \sim 0.25$ , corresponding to  $\sim 0.65$  mag of extinction ( $A_{\text{H}\alpha}$ ) and  $A_V \sim 0.8$  mag.

We collapsed the data cube in 2D flux maps and found that the  $\text{H}\alpha$  flux maps are well described by a 2D exponential profile (Figure S3). We find that the galaxy has a disk scale length of  $R_d = 0.27 \pm 0.02''$  corresponding to  $2.3 \pm 0.2$  kpc. From the flux curve-of-growth  $f(< r)$ , the  $\text{H}\alpha$  half-light radius is  $R_{1/2} = 0.44 \pm 0.03''$  or  $3.6 \pm 0.3$  kpc. The [OIII] surface brightness profile gives a value identical within the errors. The [OII] surface brightness profile is poorly constrained because of the low [OII] flux, significant OH contamination in the wings of [OII], and of the lower spatial resolution ( $0.65''$  in the  $J$ -band).

### S1.3 Emission Kinematics and 3D Modeling

We extracted the velocity field and dispersion map using the code LINEFIT developed specifically for SINFONI applications (18, 34, 43). The main key features of LINEFIT are that the spectral resolution is explicitly taken into account by convolving the assumed intrinsic emission line profile and a template line shape for the effective instrumental resolution before performing the fits. Figure S4(left) shows the flux map, 2D velocity field and dispersion maps for the  $\text{H}\alpha$  line (bottom row) and the [OIII] line (top row). Both the  $\text{H}\alpha$  and the [OIII] line trace the kinematics of the galaxy.

Contrary to traditional methods to construct 2D velocity and dispersion maps (44–48), we extracted the kinematic properties of the host galaxy directly from the data cube using a 3D fitting algorithm, i.e. without collapsing the data in 2D sub-products. Essentially, for a given flux profile and a kinematic profile, we search for the best parameters that describe the data using a Markov Chain Monte Carlo (MCMC) Bayesian approach. The algorithm compares the



data with the model convolved with the Point Spread Function (PSF) and spectral Line Spread Function (LSF) and returns both the model parameter and the intrinsic 3D model, i.e. unconvolved model. This method has several advantages, such as the dynamical center is constrained by the data (and thus need not to be fixed), the creation of 2D velocity maps is not necessary, and it provides us with a ‘deconvolved’ model.

The parametric model used in the MCMC algorithm includes a geometrically thick disk with an exponential flux profile  $f(r) \propto \exp(-r/R_d)$ . The disk intrinsic thickness  $h_z$  is taken such that the edge-on axis ratio is  $q \equiv h_z/R_{1/2} = 0.2$ , corresponding to  $\sim 1$  kpc, typical of high-redshift edge-on/chain galaxies (49), and the flux profile in the direction perpendicular to the orbital plane is modeled as  $f(z) \propto \exp(-0.5 z^2/h_z^2)$ . For the disk kinematics, we used parametric description of the rotation curve  $v(r)$ . We use either (1) an arctangent curve (44),  $v(r) \equiv 2/\pi V_{\max} \arctan(r/r_p)$ , which has two parameters  $V_{\max}$  the asymptotic velocity and  $r_p$  the inner slope, or (2) an exponentially rising profile (50),  $v(r) = V_{\max}(1 - \exp(-r/r_p))$ . We will refer to these two types of rotation curve as ‘arctan’ or ‘Exp’, respectively.

The total (line-of-sight) velocity dispersion  $\sigma_{\text{tot}}$  includes three terms (added in quadrature). It includes (i) the local isotropic velocity dispersion  $\sigma_d$  driven by the disk self-gravity is  $\sigma_d(r)/h_z = V(r)/r$  for a dynamically hot thick disk (43, 51, 52), (ii) a mixing term,  $\sigma_m$ , arising from mixing the velocities along the line-of-sight for a geometrically thick disk, and (iii) an intrinsic dispersion ( $\sigma_i$ ) —often dominant— to account for the fact that high-redshift disks are dynamically hotter than the self-gravity expectation. In  $z > 1$  disks,  $\sigma_i$  is often observed to be  $\simeq 50\text{--}80\text{km s}^{-1}$  (18, 45, 46, 48, 51, 53–56).

Because the  $\chi^2$  hyper-surface is very flat, simple  $\chi^2$  optimization tends to not converge as it is very susceptible to local minima. Hence, we use a Monte-Carlo Markov-Chain optimization algorithm to optimize the parameters using flat priors on bound intervals for each of the parameters. The values (errors) of the fit parameters are taken from the median (standard deviation) of the last 1000 iterations of 5000 since convergence is usually achieved in the first 500 iterations. We tested the algorithm extensively on about 200 data cubes generated with known parameters covering a range of fluxes and seeing conditions. We find that the algorithm reproduces the input parameters within 10% for our observing conditions (integration time and PSF).

In total, the model has 10 free parameters to be determined from the data. The 10 parameters are the  $x_o, y_o, z_o$  positions,  $R_d$  exponential scale length, the total flux, inclination  $i$ , position angle PA,  $r_v$  and  $V_{\max}$  the rotation curve parameters and  $\sigma_z$  the intrinsic dispersion. The parameters determined from  $\text{H}\alpha$ <sup>1</sup> for our galaxy towards HE 2243-60 are listed in Table S3. For instance, the galaxy PA of  $\sim 55 \pm 1^\circ$  is within 20 degrees of the quasar PA which is  $42^\circ$ , implying that the QSO line-of-sight is aligned within  $\sim 20^\circ$  from the host major axis, which implies that the QSO intercepts the disk plane at a very favorable angle to study the connection between the absorption and emission kinematics. The morphological parameters (size,  $i$ , PA) derived from this global 3D fitting technique on the  $\text{H}\alpha$  data cube agree well with those derived from the 2D- $\text{H}\alpha$  flux profile (Figure S3).

---

<sup>1</sup>We did not perform the 3D analysis on the [OIII] data because it is affected by an OH-line on the red side (see Figure S1).

In Figure S4a, we show the 2D velocity and dispersion maps for  $H\alpha$  and [OIII]. In Figure S4b, we show the distributions obtained from the MCMC algorithm for two of the model parameters. The maximum circular velocity is found to be  $V_{\max} = 145 \pm 16 \text{ km s}^{-1}$ , or  $180 \pm 32 \text{ km s}^{-1}$  for the rising exponential or arctangent rotation curve, respectively. The distribution of  $V_{\max}$  values allowed by the data given our model is shown in the top panel in Figure S4b. This corresponds to a dynamical mass of  $\log(M_{\text{dyn}}[M_{\odot}]) \simeq 10.5$  within  $2 \times R_{1/2}$ . Assuming that the maximum velocity  $V_{\max}$  is a good proxy for the halo circular velocity  $V_c(\sim V_{\text{vir}})$ , the total halo mass  $M_{\text{vir}}$  is found to be  $\log(M_{\text{vir}}[M_{\odot}]) \sim 11.6$ .

The intrinsic dispersion  $\sigma_i$  required for this galaxy is large, with an average of  $\sigma_i = 157 \pm 5 \text{ km s}^{-1}$ . Interestingly, the 2D dispersion map shows a peak at  $\sim 250 \text{ km s}^{-1}$  in a location off-centered from the dynamical center, roughly on the minor axis as shown in Figure S4a. The range of  $\sigma_i$  values allowed by the data shown in the bottom panel in Figure S4b is large compared to other rotationally supported galaxies at those redshifts (18, 45, 55, 56), which have  $\sigma_i \simeq 50\text{--}100 \text{ km s}^{-1}$ . Such a large dispersion could be the signature of a significant amount of shocked gas produced in a super-novae driven outflow (57, 58) which can leave an additional blue-shifted broad component with  $\text{FWHM} \sim 500 \text{ km s}^{-1}$ . The [OI] $\lambda$ 6300/ $H\alpha$  line ratio is perhaps the most sensitive diagnostic for shocks (59) and while we do not detect the [OI] $\lambda$ 6300 line directly, we find an upper limit of  $f_{[\text{OI}]} \lesssim 1.0 \times 10^{-17} \text{ erg s}^{-1} \text{ cm}^{-2}$ , leading to a flux ratio [OI]/ $H\alpha = 0.1$ , typical for star-forming galaxies. Because, the shock velocities required for having a [OI]/ $H\alpha$  ratio departing from the locus of star-forming galaxies is  $\gtrsim 250\text{--}300 \text{ km s}^{-1}$  (58, 59), the [OI]/ $H\alpha$  ratio is consistent with both star-formation and a mild shock with a shock speed  $v_{\text{sh}}$  which is similar to our dispersion of  $\sim 150 \text{ km s}^{-1}$ .

## S2 Absorbing gas properties

### S2.1 High-resolution spectroscopy of the quasar HE 2243–60

We combined observations of archival VLT/UVES data of the quasar HE 2243–60 ( $m_V = 18.3$ ) from several programs (ESO Program ID 065.A-0411, 067.A-0567 & 074.A-0201) (60, 61) leading to a spectrum with a very high signal-to-noise ratio (SNR). The SNR is  $\sim 110$  per  $2 \text{ km s}^{-1}$  pixel at  $4000 \text{ \AA}$  and  $6800 \text{ \AA}$  near the  $\text{Ly}\alpha$  and the  $\text{ZnII/CrII}$  absorption lines, respectively. The SNR is 40 at  $8000 \text{ \AA}$  near the  $\text{FeII}$  lines. Typical exposures were 3600 seconds long, with a total exposure time of 25,800 seconds for both the blue and red arms of the spectrograph, and a typical seeing of  $0.9''$ . The slit widths used were  $0.8''$  and  $1.0''$  wide.

The raw 2D echelle spectra were reduced using the Common Pipeline Language UVES pipeline (version 4.2.3). After performing basic steps like bias subtraction and flat-fielding, the pipeline optimally extracts the quasar spectra and their  $1\text{-}\sigma$  statistical error spectra by modeling the spatial profile of the quasar flux on the 2D frames as a Gaussian. The same profile was used to optimally extract the ThAr calibration frames and an optimized ThAr line-list (62) was used to determine a wavelength solution for the quasar frames. The extracted quasar flux was

corrected for the spectrograph’s blaze function using the flat-field frames, ensuring that the flux in overlapping portions of neighbouring echelle orders had approximately the same shape. The extracted flux from all echelle orders, from all exposures, was placed in a vacuum–heliocentric wavelength scale and combined with inverse-variance weighting and a cosmic ray/bad pixel rejection algorithm using the custom-written code `UVES_POPLER`<sup>2</sup>. This code also performed an automated continuum fit which was subsequently improved in some sections with a manual polynomial fitting routine. The final spectrum of HE 2243–60 (Figure S5) has a wavelength coverage of 3080–10,430 Å with two gaps between 8528–8663 Å and 10,256–10,261 Å. It was re-dispersed to a velocity dispersion of 2.0 km/s/pixel and has a resolving power of  $R \sim 50,000$ .

## S2.2 Metallicity and Kinematics of the absorbing gas

We present here our analysis of the absorbing gas properties (kinematics, metallicity, dust properties) using the low-ionization ions and the knowledge of the systemic redshift of the host. The exquisite high SNR VLT/UVES spectra combined with the galaxy properties revealed by the VLT/SINFONI data have enhanced dramatically our ability to interpret the physical properties of the gas associated with the host galaxy.

The VLT/UVES spectrum of HE 2243–60 is shown in Figure S5a for the Lyman series and in Figure S5b for some of the low-ionization ions. We fit all the metal lines (Zn II, Cr II, Fe II, Si II, Ni II) with multiple components using VPFIT version 9.5<sup>3</sup>. The total Si II and Zn II column densities are  $\log N(\text{Si II})[\text{cm}^{-2}] = 15.41 \pm 0.05$  and  $\log N(\text{Zn II})[\text{cm}^{-2}] = 12.53 \pm 0.05$  and the other elements are listed in Table S4. We identified 7 regions (labeled 0 to 6) that can be distinguished kinematically. For instance, there is a strong component at  $\sim 180 \text{ km s}^{-1}$  and a number of sub-components with velocities ranging from 20 to 160  $\text{km s}^{-1}$ . Figure S5b (panels a, b) shows that the Si II gas column density is contained mostly in components 2 and 4, where each have approximately 50% of the total column density.

We simultaneously fit the Ly $\alpha$ , Ly $\beta$ , Ly $\delta$  and Ly $\epsilon$  absorption in the UVES spectrum (Figure S5a) using VPFIT by scaling the Si II column densities of each of the VPFIT components and keeping the same  $b$ -parameter values. We find the total H I column density to be  $\log N_{\text{H I}}[\text{cm}^{-2}] = 20.62 \pm 0.05$ , well above the 20.3 threshold value for DLAs, indicating that the gas is likely to be almost entirely neutral. This column density is consistent with the value, 20.67, from the earlier spectra (14). In our measurement, the main source of error is from the continuum uncertainty around the Ly $\alpha$  through. Unfortunately, the VLT/UVES spectrum does not allow us to estimate the H I column in each of the components, preventing us from performing a photo-ionization analysis, because the Lyman series lines we detect are all heavily saturated. However, under the conservative assumption of constant metallicity across the profile, we use the Si II column density profile as a proxy for the H I distribution among the fitted absorption components, and

<sup>2</sup>Written and maintained by MTM at [http://astronomy.swin.edu.au/~mmurphy/UVES\\_popler](http://astronomy.swin.edu.au/~mmurphy/UVES_popler).

<sup>3</sup>VPFIT is maintained by R.F. Carswell at <http://www.ast.cam.ac.uk/~rfc/vpfit.html>.

estimate that  $\sim 50\%$  of the total HI column density of  $\log N_{\text{H}} \simeq 20.6$  is contributed by components 1–3.

Using the HI column and the refractory element least depleted on dust grains Zn, the global metallicity is estimated to be

$$[\text{Zn}/\text{H}] = -0.72 \pm 0.05. \quad (3)$$

Similarly, the Fe abundance is  $[\text{Fe}/\text{H}] = -1.13 \pm 0.06$ . These measurements are 0.3 dex larger than the original values (14) ( $[\text{Zn}/\text{H}] \simeq -1.10$ ) based on a shallower spectrum. For DLAs, this metallicity range is in the upper quartile of samples of DLAs (63–67). More importantly, for the purpose of understanding this galaxy-quasar pair, we find that the gas metallicity at 26 kpc is much smaller than that of the ISM of the host, which is  $\sim 1/3 Z_{\odot}$  (Eq. 2). Taking this comparison at face-value, this decrease of  $\sim 0.5$  dex in metallicity over 26 kpc excludes the possibility that the gas probed by the QSO line-of-sight traces entrained material in an outflow. Indeed, in such a scenario the outflow metallicity would be either enriched with metals (19, 68) or be that of the ISM.

We now turn to our analysis of the low-ionization ions across the profile. Figure S5b (panel c) shows the line ratios  $[\text{Fe}/\text{Zn}]$ ,  $[\text{Cr}/\text{Zn}]$ , and  $[\text{Si}/\text{Zn}]$  as triangles, squares and circles, respectively. Overall, one sees little depletion for Si compared to Zn, and that Cr and Fe are more depleted, as one might have expected. More interestingly, the three ion ratios show a clear trend with velocity where the regions at the highest velocities are more depleted. From these line ratios, we use the correlation between extinction  $A_V$  and dust-phase metallicity (23) to estimate the total extinction  $A_V$ . The resulting  $A_V$  profiles (Figure S5b, panel d) shows that most of the dust is located in the components with velocities  $v = 150\text{--}200 \text{ km s}^{-1}$ . Similarly, using the Jenkins method (70), one can extract a constraint on  $N_{\text{HI}} + \log Z$ , the sum of the metallicity and the gas column. We find that this quantity follows the derived  $A_V$  values very closely.

This dust profile shown in Figure S5b would mean that the gas metallicity is higher for component no. 4 than for the gas with small line-of-sight velocities (components no 1 to 3), assuming a constant dust-to-metal ratio. Thus, if we assume that the metallicity is lower in the low velocity components (no 1 to 3), this would imply that the contribution to the total  $N_{\text{H}}$  from the accreting components will be larger than the 50% value because the  $N(\text{Si})$  is similar for the two groups and that the estimated accretion rate should be revised upwards.

Finally, we note that the high-ionization ions (e.g. CIV, OVI) associated with this system have a kinematic profile (61, 69) that is very different: contrary to the low-ionization gas, it is symmetric around the galaxy systemic velocity. These could be the signatures of the virial shocks.

### S3 Kinematic modelling

Given our tight geometric constraints on the quasar apparent location with respect to the galaxy, we can simulate UVES profiles for various physical scenarios using simplified toy models. We use a Monte Carlo approach where typically  $10^5$  ‘clouds’ are created to fill these geometric configurations with simplified kinematics, which allows us to generate any sight-line absorption profile for any quasar location. Because of the random nature of the Monte Carlo approach, there will be irregularities in the simulated profiles (Figures 1d, S6). The absorption profile is generated with velocity bins given by the UVES pixel size and convolved with the instrument Line-Spread-Function.

Figure S6 shows three such toy models, namely that of accretion, a bi-conical wind, and disk, in a, b, and c, respectively. The left (middle) panels in Figure S6 show a side (front) view of the toy models, respectively. The middle panels show the average line-of-sight  $V_z$  velocity and the right panels show the simulated UVES absorption profiles for our quasar-galaxy configuration.

For the disk model, we assume a flat rotation curve, for the outflow model, we assume a constant radial outflow speed, and for the accretion model a constant inflow speed (radial) representing a non-zero mass flux. In all cases, we assume an axis symmetry around the rotation axis. For the accretion and outflow, we ensure mass conservation. While the true physical situation is likely to be more complex, this exercise shows that one can reproduce the kinematics of components no 1 to 3 with an accreting gas, while the outflow model fails to account for the kinematics of the low velocity gas unless the cone opening angle is  $> 140^\circ$ , which is not consistent with current constraints at  $z = 0.01$ –1 on the cone opening angle (20–22). Moreover, an outflow occurring in such a wide cone will lead to a kinematic profile very different from the one observed: it will have a peak at some velocity (say  $200 \text{ km s}^{-1}$ ) given by the outflow speed and a continuous decrease to about  $100 \text{ km s}^{-1}$ , leaving the components at 0 to  $100 \text{ km s}^{-1}$ , unaccounted for.

For the accretion model, one may use various geometric configurations, such a flat cylindrical, a torus-like cone (Figure S6a), or a disk-like geometry (Figure 1d) as these lead to similar kinematic profile. One may want to relax our assumption of radial orbits as the material is more likely to spiral inwards. This will introduce a small correction in Eq. 1, a correction of order unity  $\mathcal{O}(1)$  from the sine or cosine projection factor from the spiral opening angle. Hence, the resulting accretion rate could be smaller by a factor of two to three. Nonetheless, our accretion toy model represents halo gas that could be spread over 10–15 kpc (above and below the disk). This situation is similar to local examples. Indeed, in local galaxies, such as NGC 891, 21 cm observations (72) have revealed large amounts of extra-planar neutral gas in the halos of galaxies, with scale heights as large as 20 kpc. In these local examples, an inflow component of low-angular momentum gas is usually required in order to account for the kinematics seen in the 21 cm IFU data (73).

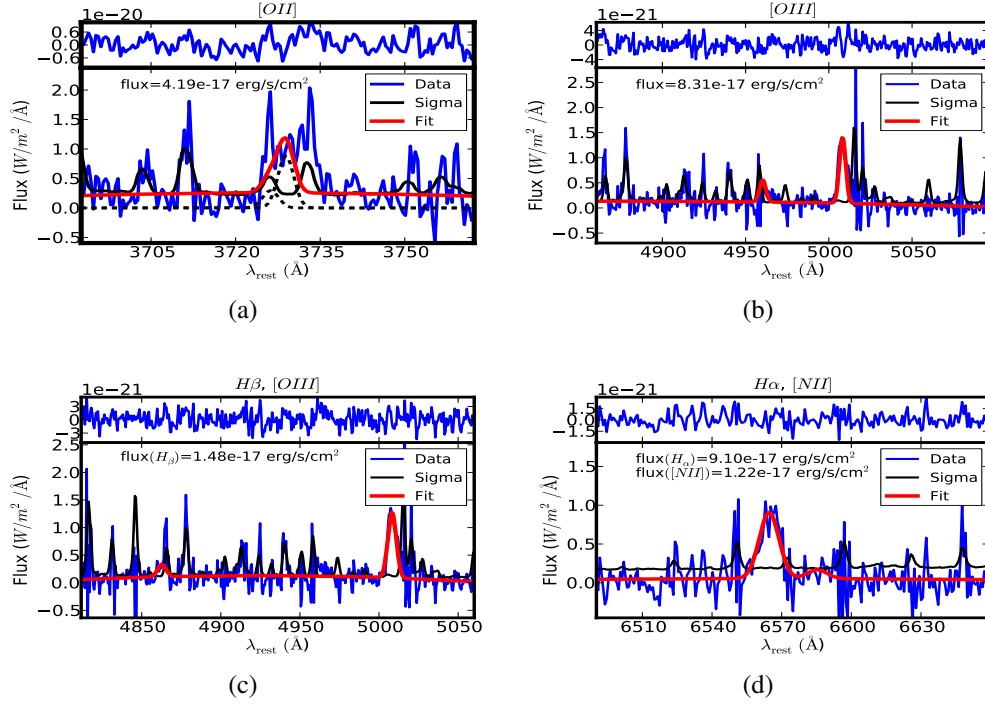


Figure S1: The SINFONI 1D-spectra extracted in a  $1.25''$  radius aperture. **(a)**  $J$ -band [OII] spectra. **(b)**  $H$ -band [OIII] spectra. **(c)**  $H$ -band  $H\beta$  spectra. **(d)**  $K$ -band  $H\alpha + [NII]$  spectra. In each panel, the data is represented by the blue lines, the error vector by the black line, and the fitted emission line(s) is shown by the thick red line. For each spectrum, the top sub-panel shows the residuals. The total flux determined from the fit is labeled. The two components of the [OIII] $\lambda\lambda 4959, 5007$  and the [OII] $\lambda\lambda 3725, 3727$  doublets are fitted simultaneously. The two components of the [OII] doublet are shown with the dashed lines. For  $H\beta$ , a joint fit is performed jointly with [OIII] $\lambda 5007$ . For [NII] $\lambda 6584$ , a joint fit is performed with  $H\alpha$ . Note the presence of OH line in the [OII] and [OIII] lines.

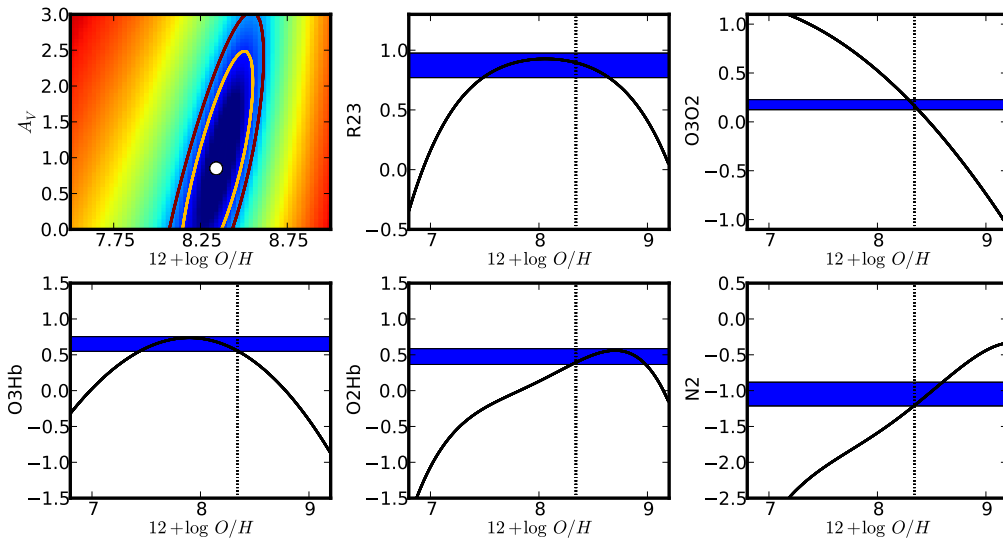


Figure S2: Galaxy Metallicity and Extinction. Using five metallicity indicators (R23, O3O2, O3Hb, O2Hb, N2), we fit simultaneously the metallicity and the extinction. The color map shows the  $\chi^2$  surface, with the  $1\sigma$  and  $2\sigma$  levels shown as contours. The fitted metallicity is found to be  $12 + \log O/H = 8.35 \pm 0.10$  and the fitted extinction is  $E(B - V) \sim 0.25$ , corresponding to  $A_V \sim 0.8$  and  $A_{H\alpha} = 0.65$ .

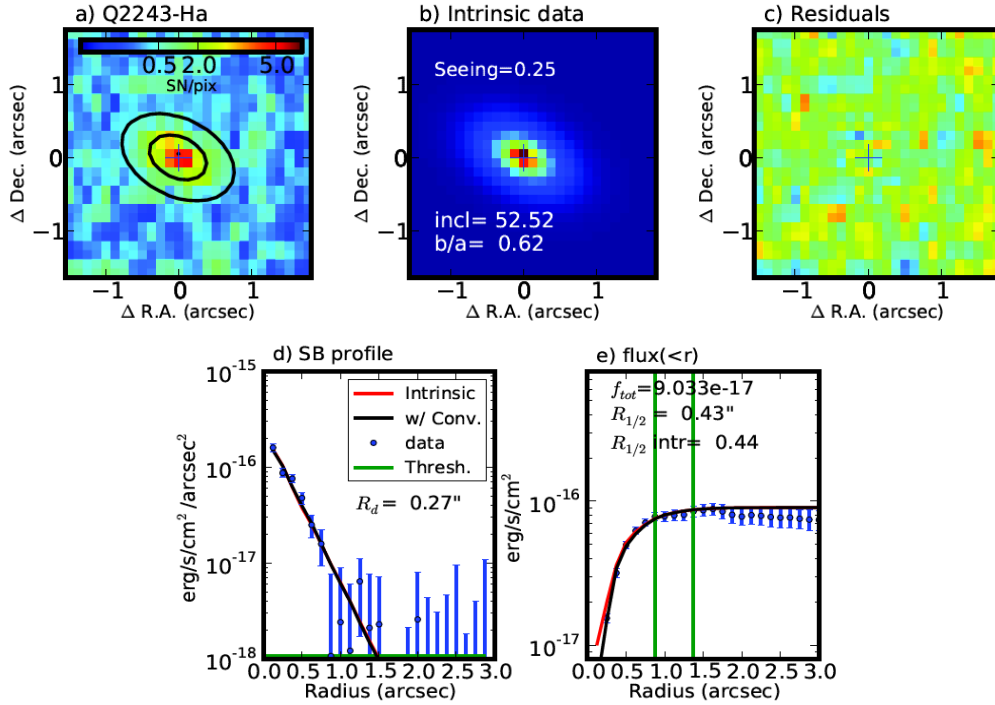


Figure S3: Flux Map and Surface Brightness Profile. From the observed  $H\alpha$  flux map shown in **a**, we fitted an exponential profile convolved with a Gaussian seeing of  $\text{FWHM}=0.25''$  **b**, whose residuals are shown in **c**. In **a**, the color scale shows the SNR per pixel and the flux contours are shown. The surface-brightness profile summed over annuli of increasing radius is shown in **d** and the corresponding growth curve  $f(<r)$  profile is shown in **e**. In (d) and (e), the intrinsic (convolved) profiles are shown in red (black) respectively. The data is represented by the filled circles with error bars. The errorbars are determined from bootstrap Monte Carlo resampling. The horizontal green line in (d) shows the threshold where the SNR reaches unity. The annuli where SNR reaches unity defines the region from where we estimate the total flux ( $f_{\text{tot}}$ ) shown as the vertical green lines in panel (e).



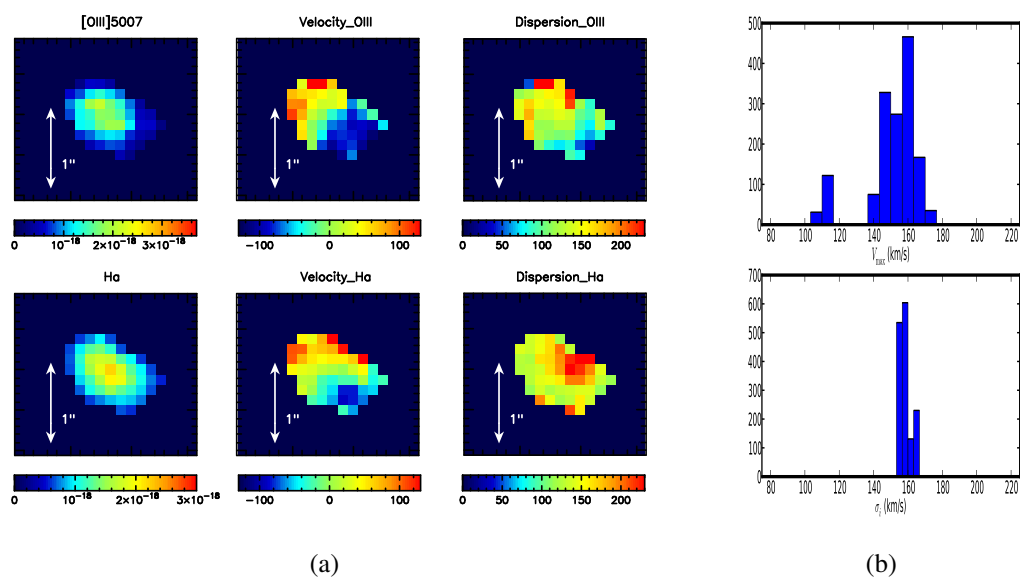


Figure S4: Kinematic analysis of the  $z = 2.328$  galaxy. For the galaxy towards HE2243–60, **a** shows the flux map ( $\text{erg s}^{-1} \text{cm}^{-2}$ ), velocity field ( $\text{km s}^{-1}$ ) and dispersion map ( $\text{km s}^{-1}$ ) are shown on the left, middle, right panels. The H $\alpha$  ([OIII]) maps are shown in the bottom (top) row, where the FWHM of the PSF is  $0.25''(0.4'')$ , corresponding to  $\sim 2 \text{ kpc}$  ( $3.3 \text{ kpc}$ ), respectively. In **b**, from our Markov chains on our 3D model parameters, we show distributions allowed by the data on the (intrinsic) maximum circular velocity  $V_{\max}$  and the intrinsic dispersion ( $\sigma_i$ ) parameters (using the arctangent model for the rotation curve).

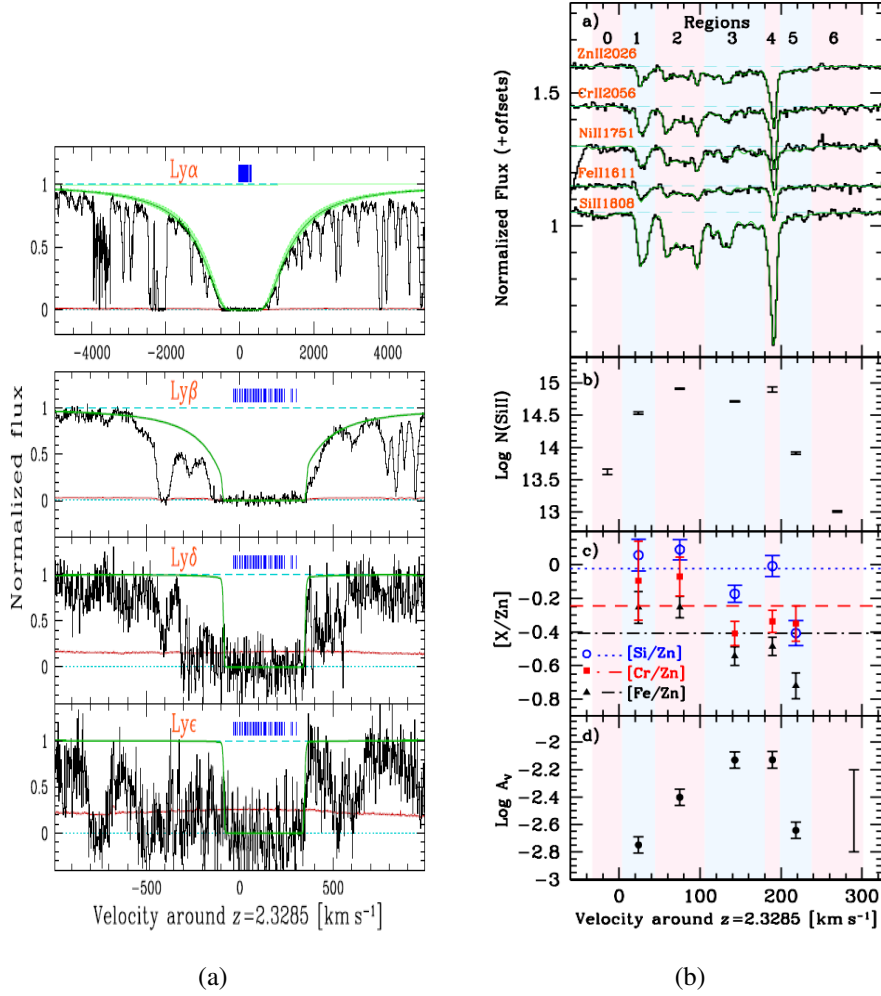


Figure S5: High-resolution VLT/UVES spectrum of HE2243–60. **a** Spectrum covering the Lyman series. We simultaneously fit the Ly $\alpha$ , Ly $\beta$ , Ly $\delta$  and Ly $\epsilon$  absorption in the UVES spectrum using VPFIT by scaling the SiII column densities of each of the components and keeping the same  $b$ -parameter values. Lyman series lines we detect are all heavily saturated, which prevents us from measuring the HI column density in the sub-regions (1 to 6) directly. **b** Spectrum covering the low-ionisation ions. In panel a we show the low-ionisation ions (ZnII, CrII, FeII, SiII, NiII) associated with the DLA host galaxy. We fit each ion with multiple components using VPFIT and identified 7 regions (labeled 0 to 6) that can be distinguished kinematically. The galaxy systemic redshift corresponds to 0 km s $^{-1}$ . Panel b shows the SiII column density profile across the seven regions. The gas is distributed roughly equally between the components 0–3 and 4–6. From the ion ratios ([Si/Zn], [Cr/Zn], [Fe/Zn]) (panel c) and the corresponding gas extinction  $A_V$  (panel d), we see an increasing amount dust depletion towards the components 3 and 4. Error bars show the measurement errors and the systematic uncertainty is shown at  $v = 290$  km s $^{-1}$ .

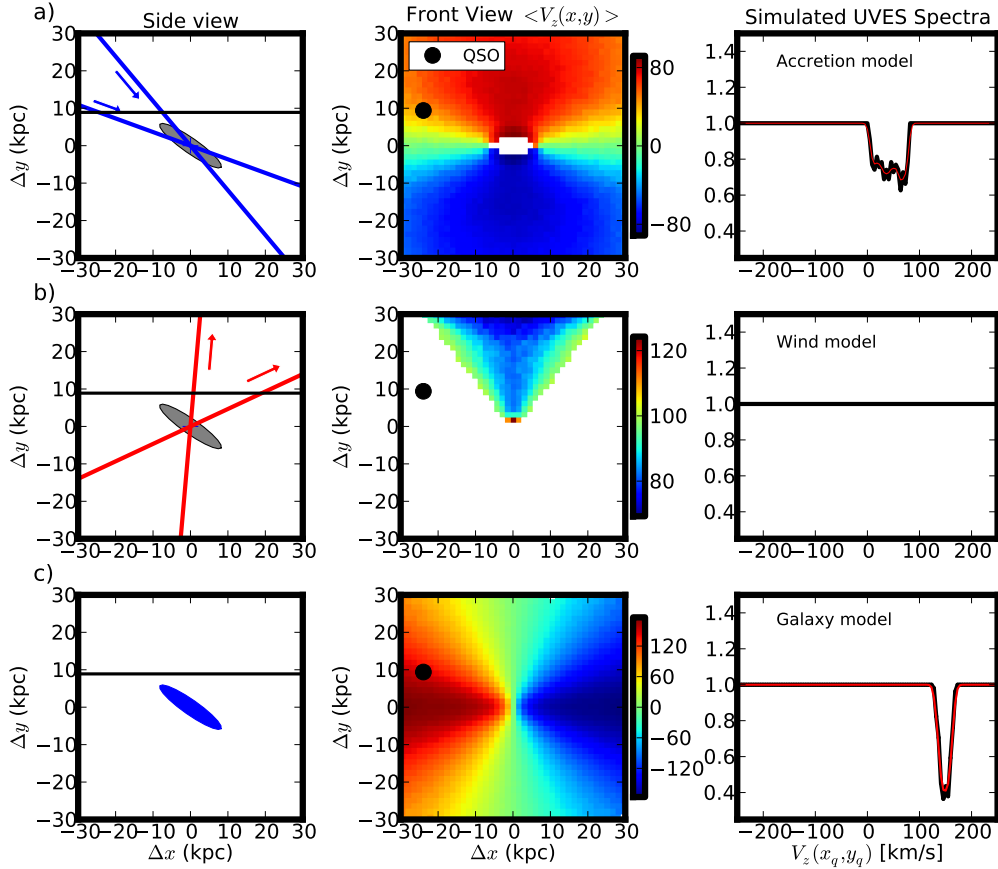


Figure S6: Simulated line-of-sight kinematics for various components. The accretion, outflow and disk components are shown in **a**, **b** and **c**, respectively. For each components of the modeling (disk, outflow, inflow), we show a side view (left), a front view of the average line-of-sight velocity (middle) and a simulated spectra at the UVES resolution (right). For typical opening angles of  $60^\circ$ , a bi-conical outflow does not intercept the sight-line. A simple accretion model with a non-zero radial component can account for the intermediate velocities seen in the VLT/UVES spectra (components 1-3 in Figure 1, S5) between 0 and  $100 \text{ km s}^{-1}$ .

Table S1: Journal of the VLT/SINFONI Observations.

Instrument	Mode	Grating	Pixel (")	$t_{\text{exp}}$ (s)	PSF FWHM (")	Run ID
SINFONI	NGS	K	0.125×0.25	12000	0.25	383.A-0750
SINFONI	NGS	H	0.125×0.25	12000	0.4	383.A-0750
SINFONI	NGS	J	0.125×0.25	10800	0.65	088.B-0715

Table S2: Summary of the host emission properties.

Line	Flux ( $\text{erg s}^{-1} \text{cm}^{-2}$ ) ( $\times 10^{-17}$ )
$\text{H}\alpha$ $\lambda 6564$	9.1(0.2)
$[\text{N II}]$ $\lambda 6583$	<1.22
$\text{H}\beta$ $\lambda 4963$	1.7(0.4)
$[\text{O I}]$ $\lambda 6300$	<1.15
$[\text{O II}]$ $\lambda 3727$	3.8(0.4)
$[\text{O III}]$ $\lambda 5007$	8.1(0.2)

Table S3: Summary of the host kinematics properties. We use two or three-dimensional fits on the H $\alpha$  data cube to determine the galaxy size and kinematic parameters. We use an exponential flux profile and for the 3D fits the rotation curve  $f_V(r)$  is assumed to be either a rising exponential ('Exp') or an arctangent ('arctan').

Fit	$f_V(r)$	$R_d$ (kpc)	$i$ (deg)	PA (deg)	$r_p$	$V_{\max}$ (km s $^{-1}$ )	$\sigma_i$ (km s $^{-1}$ )
2D	n.a.	2.30(0.15)	54(4)	62(6)	...	...	...
3D	arctan	2.37(0.05)	55(1)	54(1)	1.22(0.5)	145(16)	157(5)
3D	Exp.	2.30(0.05)	53(1)	55(1)	3.5(0.6)	180(32)	158(5)

Table S4: Column densities and Abundances Measurements.

X	$\log N_X$	[X/H]	Reference
(1)	(2)	(3)	(4)
H	$20.62 \pm 0.05$	N.A.	This work
CrII	$13.31 \pm 0.01$	$-0.96 \pm 0.06$	This work
FeII	$14.96 \pm 0.01$	$-1.13 \pm 0.06$	This work
NiII	$13.88 \pm 0.01$	$-0.96 \pm 0.05$	This work
SiII	$15.41 \pm 0.01$	$-0.74 \pm 0.07$	This work
ZnII	$12.53 \pm 0.01$	$-0.72 \pm 0.05$	This work
O	16.21	$-0.92 \pm 0.22$	(14)
OVI	14.98	...	(69)
CIV	14.73	...	(69)
NV	13.50	...	(71)
NI	14.59	...	(71)

(1) Element name; (2) Column density; (3) Abundances; (4) References.

## References

31. J. Schreiber, *et al.*, *ASP Conf. Ser. 314: Astronomical Data Analysis Software and Systems (ADASS) XIII*, F. Ochsenbein, M. G. Allen, D. Egret, eds. (2004), p.380.
32. R. Abuter, *et al.*, *New Astronomy Review* **50**, 398 (2006).
33. R. Davies, *MNRAS* **375**, 1099 (2007).
34. N. M. Förster Schreiber, *et al.*, *ApJ* **645**, 1062 (2006).
35. N. Bouché, *et al.*, *ApJ* **669**, L5 (2007).
36. G. Chabrier, *PASP* **115**, 763 (2003).
37. D. Calzetti, *et al.*, *ApJ* **533**, 682 (2000).
38. L. J. Kewley, M. A. Dopita, *ApJS* **142**, 35 (2002).
39. R. Maiolino, *et al.*, *A&A* **488**, 463 (2008).
40. C. Allende Prieto, D. L. Lambert, M. Asplund, *ApJ* **556**, L63 (2001).
41. G. Cresci, *et al.*, *Nat* **467**, 811 (2010).
42. F. Mannucci, G. Cresci, R. Maiolino, A. Marconi, A. Gnerucci, *MNRAS* **408**, 2115 (2010).
43. R. Davies, *et al.*, *ApJ* **741**, 69 (2011).

44. M. Puech, *et al.*, *A&A* **484**, 173 (2008).
45. G. Cresci, *et al.*, *ApJ* **697**, 115 (2009).
46. S. A. Wright, *et al.*, *ApJ*, (*arXiv:0810.5599*) (2009).
47. B. Epinat, *et al.*, *A&A* **504**, 789 (2009).
48. B. Epinat, P. Amram, C. Balkowski, M. Marcelin, *MNRAS* **401**, 2113 (2010).
49. B. G. Elmegreen, D. M. Elmegreen, *ApJ* **650**, 644 (2006).
50. J. Q. Feng, C. F. Gallo, *Research in Astronomy and Astrophysics* **11**, 1429 (2011).
51. R. Genzel, *et al.*, *ApJ* **687**, 59 (2008).
52. J. Binney, S. Tremaine, *Galactic Dynamics: Second Edition* (Princeton University Press, 2008).
53. D. R. Law, *et al.*, *ApJ* **669**, 929 (2007).
54. B. Epinat, *et al.*, *A&A* **539**, A92 (2012).
55. E. Wisnioski, *et al.*, *MNRAS* **417**, 2601 (2011).
56. D. R. Law, *et al.*, *Nat* **487**, 338 (2012).
57. S. F. Newman, *et al.*, *ApJ* **752**, 111 (2012).
58. K. T. Soto, C. L. Martin, *ApJS* **203**, 3 (2012).
59. M. A. Dopita, R. S. Sutherland, *ApJ* **455**, 468 (1995).
60. P. Noterdaeme, *et al.*, *A&A* **474**, 393 (2007).
61. A. J. Fox, C. Ledoux, P. Petitjean, R. Srianand, *A&A* **473**, 791 (2007).
62. M. T. Murphy, P. Tzanavaris, J. K. Webb, C. Lovis, *MNRAS* **378**, 221 (2007).
63. V. P. Kulkarni, S. M. Fall, *ApJ* **580**, 732 (2002).
64. J. X. Prochaska, E. Gawiser, A. M. Wolfe, J. Cooke, D. Gelino, *ApJS* **147**, 227 (2003).
65. P. Khare, *et al.*, *A&A* **464**, 487 (2007).
66. S. L. Ellison, N. Kanekar, J. X. Prochaska, E. Momjian, G. Worseck, *MNRAS* **424**, 293 (2012).



67. M. Rafelski, A. M. Wolfe, J. X. Prochaska, M. Neeleman, A. J. Mendez, *ApJ* **755**, 89 (2012).
68. C. L. Martin, H. A. Kobulnicky, T. M. Heckman, *ApJ* **574**, 663 (2002).
69. A. J. Fox, P. Petitjean, C. Ledoux, R. Srianand, *A&A* **465**, 171 (2007).
70. E. B. Jenkins, *ApJ* **700**, 1299 (2009).
71. A. J. Fox, *et al.*, *A&A* **503**, 731 (2009).
72. T. Oosterloo, F. Fraternali, R. Sancisi, *ApJ*, **134**, 1019 (2007).
73. F. Fraternali, J. J. Binney, *MNRAS*, **386**, 935 (2008).